# Stimuli-sensitive linear-dendritic block copolymer-drug prodrug as nano-platform for tumor combination therapy

*Hao Cai, Ping Tan, Xiaoting Chen, Michal Kopytynski, Dayi Pan, Xiuli Zheng, Lei Gu, Qiyong Gong, Xiaohe Tian, Zhongwei Gu, Hu Zhang, Rongjun Chen, Kui Luo**

Dr. H. Cai, Dr. P. Tan, Dr. D. Y. Pan, Dr. X. L. Zheng, L. Gu, Prof. Q. Y. Gong, Prof. X. H. Tian, Prof. Z. W. Gu, Prof. K. Luo
Huaxi MR Research Center (HMRRC), Department of Radiology, National Clinical Research Center for Geriatrics, Frontiers Science Center for Disease-Related Molecular Network, State Key Laboratory of Biotherapy, West China Hospital, Sichuan University, Chengdu 610041, China. *E-mail: luokui@scu.edu.cn

X. T. Chen
Animal Experimental Center of West China Hospital, Sichuan University, Chengdu, 610041, China

Dr. R. Chen, Dr. M. Kopytynski
Department of Chemical Engineering, Imperial College London, South Kensington Campus, London SW7 2AZ, United Kingdom

Prof. H. Zhang
Amgen Bioprocessing Centre, Keck Graduate Institute, Claremont, CA 91711, USA

Prof. Q. Y. Gong, Prof. K. Luo
Functional and Molecular Imaging Key Laboratory of Sichuan Province, and Research Unit of Psychoradiology, Chinese Academy of Medical Sciences, Chengdu, 610041, China

**Keywords**: tumor microenvironment-responsive, linear-dendritic block copolymer, amphiphilic polymer, nanomedicine, combination therapy

**Abstract**: Linear-dendritic block copolymer (LDBCs) are highly attractive candidates for smart drug delivery vehicles. Herein, we report an amphiphilic poly[(ethylene glycol) methyl ether methacrylate] (POEGMA) linear-peptide dendritic prodrug of doxorubicin (DOX) prepared by reversible addition-fragmentation chain transfer (RAFT) polymerization. A hydrophobic dye-based photosensitizer chlorin e6 (Ce6) was employed for encapsulation in the prodrug nanoparticles (NPs) to obtain a LDBCs-based drug delivery system (LD-DOX/Ce6) which offered a combination cancer therapy. Due to the presence of Gly-Phe-Leu-

Gly peptides and hydrazone bonds in the prodrug structure, LD-DOX/Ce6 were degraded into small fragments, thus specifically triggering the intracellular release of DOX and Ce6 in the tumor microenvironment. Bioinformatics analysis suggested that LD-DOX/Ce6 with laser irradiation treatment significantly induced apoptosis, DNA damage and cell cycle arrest. The combination treatment could not only suppress tumor growth, but also significantly reduced tumor metastasis compared with treatments with DOX or Ce6 through regulating EMT pathway, TGFβ pathway, angiogenesis and the hypoxia pathway. LD-DOX/Ce6 displayed a synergistic chemo-photodynamic anti-tumor efficacy, resulting in a high inhibition in tumor growth and metastasis, while maintaining an excellent biosafety. Therefore, this study has demonstrated potential of the biodegradable and tumor microenvironment-responsive LDBCs as an intelligent multifunctional drug delivery vehicle for high-efficiency cancer combination therapy.

## 1. Introduction

Although stimuli-responsive polymer-based nano drug delivery systems (NDDSs) have a substantial clinical potential, their tunable properties can be further improved via optimization of the chemical composition, molecular structure and molecular weight (MW).[1] Encapsulation or conjugate of multiple drugs into a rationally designed multifunctional polymeric carrier can increase drug solubility and stability and enable tumor targeting through the enhanced permeability and retention (EPR) effect, thereby minimizing toxic side effects, and resulting in enhanced therapeutic indexes owing to the combination therapy.[2] Traditional polymer structures investigated for drug delivery and combination cancer therapy are mostly linear amphiphilic block polymers, which are relatively simple in structure and difficult to modify in function.[3] In the last decade, dendritic polymers, including dendrimers, dendrons, dendronized polymers and branched polymers, have been studied as alterative polymeric carriers owing to their surface functionality, globular conformation and nanoscale sizes.[4] However, several shortcomings have limited their use for cancer therapy.[5] In general, the therapeutic agents are mainly physically encapsulated into the internal cavity of the dendrimers or chemically coupled to the dendritic surface.[6] For the physical encapsulation method, high-generation dendrimers are difficult to prepare and have poor biocompatibility, while low-generation dendrimers are not dense enough to retain drugs under sink conditions, leading to inevitable burst release. Using chemical conjugation methods, surface modification often requires cumbersome synthesis steps, and will change the physicochemical properties, such as the solubility of the dendrimers. In addition, low-generation dendrimers usually have a small particle size (< 20 nm), which makes them easily removed by glomerular filtration.[7]

With the advancement of synthetic chemistry technologies, polymer architectures have evolved from linear and dendritic to more complex, branched topologies, thereby providing further opportunities for improved cancer treatment. Based on the characterization of linear and dendritic polymers, linear-dendritic block copolymers (LDBCs), a new type of polymer structure combining topological characteristics of branched chains and self-assembly properties of block copolymers, hold unique advantages in the development of drug delivery systems with micelle-like structures.[8] The linear and dendritic/branched structural units of LDBCs can offer multi-valency for loading therapeutic agents, conferred by dendrons, and conformational flexibility, conferred by linear units. Thereby, LDBCs have versatile dendritic structures and controllable self-assembly properties, enabling encapsulation or conjugation of a variety of therapeutic agents for combination treatment of tumors.

There have been some reports on the development of LDBCs as novel drug delivery systems.[8b, 9] Benefitting from the functionalization and special structural characteristics of dendritic blocks, LDBCs have significantly improved drug delivery efficiency and therapeutic effects compared to their linear analogs.[10] So far, LDBCs are mainly prepared by the coupling strategy, the “chain-first” strategy or the “dendron-first” strategy, and the synthesis method highly depends on the efficient click reaction or the gradual polymerization of macromolecules.[8a] For example, poly(ethylene glycol) (PEG) is one of the most commonly used linear polymer chains in the preparation of LDBCs, because of its good hydrophilicity and structural flexibility.[11] However, linear mPEG or PEG usually has only one or two reaction sites at ends for conjugation, and the entanglement of high MW PEG chains causes steric hindrance, resulting in a low reaction efficiency in the preparation of LDBCs by the coupling strategy, because it needs direct coupling of the synthesized dendron with the linear chain. The MW of PEG used in the LDBCs reported by other researchers is usually 5 kDa or 10 kDa.[10c, 12] Therefore, due to the considerations of drug loading capacity, solubility and self-assembly performance, this relatively low MW range of hydrophilic segments may limit the choice of hydrophobic segments in LDBCs. In addition, for LDBCs synthesized through the “chain-first” route, the preparation of a high-generation dendron requires a large number of end group conversions, which requires extremely high-yield reactions, otherwise it will cause structural defects. Meanwhile, due to the inevitable shielding effect of the polymer chain, the synthesis process is more complicated, making it difficult to characterize the product.[4c]

Recently, reversible addition-fragmentation chain-transfer (RAFT) polymerization has been widely used to synthesize linear polymers with controlled MWs, narrow MW dispersity and

precise functions due to its ease of use and compatibility with a wide range of monomers.[13] Poly (ethylene glycol) methyl ether methacrylate (POEGMA) prepared via RAFT polymerization have much higher MWs, high hydrophilicity, and structure flexibility of PEG. In addition, the obtained hydrophilic segment has high polymerization activity and can be used in subsequent polymerization reactions.[14] Thus, the POEGMA may overcome the drawbacks of linear PEG chains and the immunogenicity of PEG,[15] which provided possibility for preparing advanced LDBC-based drug delivery systems. In addition, dendritic components in LDBCs also have a crucial influence on their multifunctionalities, as well as self-assembly and stimuli-responsive behavior. Peptide dendrimers prepared by step-by-step organic synthesis have been reported and have excellent biological safety and modifiable properties.[16] Therefore, controlling the structure and topology of multifunctional LDBCs can unlock their unique advantages for efficient drug delivery. Previously, we prepared low MWs functionalized polymers via RAFT polymerization and chemical modification. The dendronized polymers demonstrated significantly improved pharmacokinetic properties and therapeutics indexes owing to their enhanced MWs and structure multivalent effect.[17]

Herein, we address the challenges in synthesis of PEG-based LDBCs, provide a new strategy for preparing LDBC-based drug delivery systems and use them for combination cancer therapy. The novel linear-dendritic block polymer is obtained by direct RAFT polymerization of dendron-based monomer using POEGMA as a macromolecular chain transfer agent (macroCTA). As shown in Schemes S1-S4, a class of cathepsin B and pH-dual sensitive LDBC-based prodrugs were designed and prepared using POEGMA and multifunctional peptide dendrons as the linear and dendritic parts, respectively. Through this innovative synthetic method, the hydrophilic and hydrophobic properties, generation, functional groups and MW of peptide dendrons can be precisely controlled at the molecular level, and the chemical composition and degree of polymerization of the linear chain can also be easily adjusted. The dendritic structure was covalently attached to the linear polymer backbone via the Gly-Phe-Leu-Gly (GFLG) peptide as a hydrophobic moiety, while DOX was covalently linked to the dendron through a hydrazone bond, thereby obtaining a class of cathepsin B and pH dual sensitive LDBC-based DOX prodrug. The amphiphilic and block linear-dendritic polymer-DOX prodrug self-assembled into tumor microenvironment-responsive and biodegradable polymeric nanoparticles (NPs). Subsequently, based on the hydrophobic cavity of dendron and the self-assembly performance of the LDBCs prodrug, the hydrophobic dye-based photosensitizer, chlorin e6 (Ce6) was used for encapsulation, thereby preparing a polymer drug delivery system that can be used to simultaneously deliver DOX

and photosensitizer. The self-assembly and drug-loading mechanism was investigated through dissipative particle dynamics (DPD) simulations and experiments. In the tumor cell microenvironment, the released Ce6 generated cytotoxic reactive oxygen species (ROS) upon irradiation with a 660 nm laser, thereby producing a synergistic anti-tumor effect with the chemotherapeutic drug DOX. The self-assembly behavior, drug loading capacity, drug release profile, and the combination anticancer mechanisms were investigated. The demonstrated co-delivery of multiple therapeutic agents to tumor cells using this novel LDBC-based NDDS represents a promising platform for combination therapies to enhance therapeutic efficacies.

## 2. Results and Discussion

In order to obtain the LDBCs with optimized structure, we first synthesized a series of multifunctional polymer prodrugs with different structures and evaluated their potential as drug carriers. As shown in **Figure 1**a, among these polymer prodrugs, the chemotherapeutic drug DOX was attached to the periphery of the dendron through a hydrazone bond, while the dendron was covalently attached to the polymer backbone through a tetrapeptide (GFLG or GFGL). The GFLG linker can be cleaved in the presence of cathepsin B, which is highly expressed in a variety of tumor cells.[18] We prepared a cathepsin B low-sensitive tetrapeptide sequence GFGL-modified monomer as control to compare the differences in physicochemical properties such as drug release profiles of the polymer prodrugs (Schemes S2 and S4). In addition, different generations of dendrons were prepared to examine the influence of dendrons on the assembly properties of LDBCs (Schemes S3-S4). These DOX prodrug conjugates were synthesized through a series of steps: first, OEGMA-based macromolecular chain transfer agents (POEGMA-CTA, Scheme S3) were prepared through controlled RAFT polymerization, while the GFLG or GFGL functionalized dendrons were prepared by liquid phase synthesis. Subsequently, the macromolecular chain transfer agent POEGMA-CTA was copolymerized with MA-GFLG-NHNHBoc, MA-GFLG-$(NHNHBoc)_2$, MA-GFLG-$(NHNHBoc)_4$, MA-GFGL-NHNHBoc, MA-GFGL-$(NHNHBoc)_2$ and MA-GFGL-$(NHNHBoc)_4$, respectively, through RAFT polymerization, thereby preparing the polymer intermediates with different structures. After deprotection, the antitumor drug DOX was covalently linked to the periphery of the dendrons via a pH-sensitive hydrazone bond. Thereby a series of amphiphilic linear-dendritic polymer prodrugs were obtained (POEGMA-GFLG/GFGL-$(DOX)_x$) (where x = 1, 2 or 4 ).

The cathepsin B-responsive monomers, MA-GFLG-NHNHBoc, MA-GFLG-$(NHNHBoc)_2$ and MA-GFLG-$(NHNHBoc)_4$, and the cathepsin B low-sensitive monomers, MA-GFGL-NHNHBoc, MA-GFGL-$(NHNHBoc)_2$ and MA-GFGL-$(NHNHBoc)_4$, were synthesized and

their chemical structures were confirmed by proton nuclear magnetic resonance ($^1$H NMR) and matrix assisted laser desorption ionization time-of-light mass spectrometry (MALDI-TOF MS) (Figures S1-S30). The polymer intermediates with different structures were also confirmed by $^1$H NMR and gel permeation chromatography (GPC) (Figures S31-S33 and Table S1). As shown in Table S1, the resulting polymer intermediates had high number-average ($M_n$) molecular weights ($M_n$ > 23 kg mol$^{-1}$) and low dispersity ($Đ$ < 1.3). After deprotection, the content of DOX covalently attached to the side chains of the polymers through the hydrazone bond was determined by UV–Vis spectroscopy. As shown in Table S2, POEGMA-GFLG-(DOX)$_4$ and POEGMA-GFGL-(DOX)$_4$ showed the highest DOX loadings at 10.8% and 11.3%, respectively, compared to their analogs.

The $^1$H NMR spectra of polymer intermediates and products (Figure S32 and S33) were similar due to their similar compositions. Specifically, taking POEGMA-GFLG-(DOX)$_4$ as an example, compared with POEGMA-CTA, peaks for the dendron monomers were observed at 7.0-10.0 and 1.3 ppm, while the characteristic peak for an ethylenic bond in the functionalized monomer disappeared (Figures S34a and S34b), indicative of successful synthesis of the LDBCs by RAFT polymerization. After reaction with the carbonyl group of DOX, the peak for the -Boc group at 1.3 ppm in the POEGMA-GFLG-(NHNHBoc)$_4$ disappeared, while characteristic peaks for DOX were observed at 7.5–8.5 and 5.3 ppm (Figure S34c). In addition, a significant UV-vis absorption peak of DOX in LD-DOX was observed at 480 nm (Figure S34d), and the purity result via HPLC revealed that the polymer prodrugs did not contain free DOX (Figure S35a), confirming that DOX was successfully linked to the polymer through the hydrazone bond. The above results showed that we have successfully prepared linear-dendritic prodrugs based on POEGMA and peptide dendron.

The GFLG linker between dendron and polymer backbone could be cleaved by cathepsin B, and the hydrazone bonds between DOX and dendron can be degraded in a weakly acidic environment.[19] Therefore, in the microenvironment of tumor cells, dual-responsive polymer prodrugs were expected to rapidly degrade and release the contained DOX. To investigate the cathepsin B/pH co-triggered DOX release behaviors of polymeric prodrugs, different samples were incubated in a simulated tumor intracellular microenvironment. As shown in Figure 1b, in the presence of cathepsin B at pH 5.4, the dual-responsive polymer prodrugs POEGMA-GFLG-DOX, POEGMA-GFLG-(DOX)$_2$ and POEGMA-GFLG-(DOX)$_4$ showed a rapid drug release rate. The cumulative release of DOX within 8 h was close to 80%, which was significantly higher than that of GFGL-modified polymer prodrug (less than 50%) and the GFLG-modified polymer prodrugs incubated in the presence of cathepsin B at pH 7.4 (less

than 30%) (Figure S35b). This rapid release property can enable the drug to quickly reach a therapeutic concentration in tumor cells, thereby reducing the possibility of drug resistance.[20] Furthermore, we measured the CMC of the dual-responsive polymer prodrugs to evaluate their ability to self-assemble into NPs. As shown in Figure 1c, compared to POEGMA-GFLG-DOX and POEGMA-GFLG-$(DOX)_2$, POEGMA-GFLG-$(DOX)_4$ exhibited the lowest CMC value (2.22 μg $mL^{-1}$), suggesting that amphiphilic LDBCs modified with a higher generation dendron could improve the stability and self-assembly capacity. We then investigated the pharmacokinetic properties of different dual-response polymer prodrugs in mice. Figure 1d showed the temporal change of DOX concentration in the plasma after intravenous (i.v.) injection of three prodrugs and free DOX into mice. The derived pharmacokinetic parameters (Table S3) revealed that the POEGMA-based prodrugs significantly increased the half-life of DOX. Among them, POEGMA-GFLG-$(DOX)_4$ showed the longest blood half-life, which was 1.78 and 1.41 times that of POEGMA-GFLG-DOX and POEGMA-GFLG-$(DOX)_2$, respectively. Based on the above analysis, POEGMA-GFLG-$(DOX)_4$ (designated as LD-DOX) was chosen as an optimal carrier in the further study.

It is worth noting that LD-DOX has several significant advantages compared to the previously reported linear-dendritic polymers. First, the macromolecular chain transfer agent POEGMA-CTA has high polymerization activity, allowing it to efficiently polymerize with methacrylated dendrons. In this study, we first designed and prepared this novel LDBCs that can be obtained by one-step RAFT polymerization. The dendritic part of the LDBCs prepared by this method can covalently polymerize multiple dendritic molecules, thereby effectively avoiding the problem of fewer reaction sites in the traditional linear polymer chain. Second, peptide dendrons constituting the dendritic part of LDBCs have high biocompatibility, and their suitable generation and lower MW can reduce the steric hindrance during the reaction process and improve the polymerization efficiency. Meanwhile, the peptide dendrons are prepared through gradual organic synthesis, so their structure can be accurately controlled while also easily multifunctional, such as the cathepsin B and pH responsiveness. In addition, low-generation dendrons also effectively avoid complicated synthesis steps and possible structural defects of high-generation dendrons. Finally, the linear polymer chain structure and properties are easily adjusted by RAFT polymerization, and the resulting POEGMA has a controllable MW and low dispersity. The MW of the linear polymer chain of LD-DOX is much higher than the MW of the linear-dendritic molecule PEG reported so far, and it has high reactivity, which provides more possibilities for the choice of dendritic part for polymerization. In addition, a high proportion of hydrophilic segments is also more conducive

to the assembly of LD-DOX into stable spherical micelle-like structures, thereby improving their stability and drug loading capacity. Therefore, incorporating the merits of dendritic architectures and the advantages of block copolymers, the LD-DOX is deemed to be a promising candidate for the construction of drug delivery systems.

DPD calculations were then used to simulate the self-assembly of LD-DOX and its ability to encapsulate hydrophobic therapeutic agents. The polymer structure and molecular model of LD-DOX was shown in Figure 1e. Figure S36 depicts the process of dynamic formation of NPs from the prodrug LD-DOX in aqueous solution. Due to the presence of hydrophilic linear POEGMA and hydrophobic dendritic parts, LD-DOX first forms smaller incomplete aggregates through hydrophilic and hydrophobic interactions, followed by gradual formation of larger complete micelle-like NPs. This result indicates that the amphiphilic LDBCs-based prodrug has good self-assembly capabilities. Further DPD simulation work was carried out using a photosensitizer Ce6 to demonstrate the ability of the polymer prodrug NPs to encapsulate hydrophobic therapeutic agents (Figure 1f). Initially, the hydrophobic domain of the polymers interacts with hydrophobic Ce6 molecules to minimize the volume fraction of Ce6. Then, smaller, incomplete micelle-like aggregates form. Finally, the bigger complete micelles appear, with Ce6 encapsulated in their hydrophobic core. Furthermore, by adjusting the concentration of Ce6, we compared the formation of NPs by polymer prodrugs under different Ce6:DOX weight ratios. Figure 1g displays the snapshot of equilibrium structures self-assembled from these polymers at different Ce6:DOX feeding ratios. It can be noted that when the ratio of Ce6 to DOX does not exceed 1, polymer prodrugs and Ce6 form complete NPs. Further increasing the Ce6 concentration (DOX:Ce6 = 1:1.5, wt/wt) will result in saturation of the number of Ce6 molecules in the hydrophobic core of the micelle. Under this condition, the excess Ce6 molecules exist in the solvent in the form of colloids or precipitates.

Dynamic light scattering (DLS) and transmission electron microscope (TEM) were used to detect the size and morphology of NPs based on polymer prodrugs. As shown in Figure S37a, the DLS measurement confirmed that the LD-DOX prodrug in aqueous solution self-assembled into NPs with a hydrodynamic size of 46.82 nm. It is worth noting that, compared to the polymer prodrug LD-DOX, the Ce6-encapsulated NPs LD-DOX/Ce6 (Ce6: DOX = 1.5, wt/wt) showed a larger hydrated particle size of 67.78 nm (Figure S37b), and a regular spherical morphology was detected by TEM (Figure 1h). Further, 100,000 time steps were used to simulate the drug release process in the presence of cathepsin B at pH 5.4. As shown in Figures 1i and S38, the presence of cathepsin B and the acidic pH can cause the cleavage of GFLG peptides and hydrazone bond, respectively, leading to disintegration of the nano

structure and the consequent drug release. By examining the morphology of the LD-DOX/Ce6 after incubation at pH 5.4 for 24 h under the TEM, the structure of the NPs disintegrated in acidic conditions, displaying a loose aggregated morphology (Figure 1j). This result further demonstrated that the NPs can specifically release the loaded therapeutic agents in response to the acidic, tumor-like microenvironment. The simulated release curve showed that compared with a single response, the drug release rate was faster with a dual response to pH and the enzyme (Figures S38c and S38d). These simulations provided insights into how LDBC-based prodrugs form NPs, how Ce6 was loaded into these particles and the mechanisms by which DOX and Ce6 were released. Hydrophobic interactions were the primary driver for NPs formation and drug loading, and the disintegration of the NPs assembly structure caused by the cleavage of specific chemical bonds (GFLG peptides and hydrazone bond) was the main driving force for drug release.

The potential of LDBC-based LD-DOX prodrugs for co-delivery of hydrophobic therapeutic agents to achieve combination anti-cancer therapy was evaluated. The results for encapsulation of PTX or Ce6 into LD-DOX through the thin-film hydration method [21] were summarized in Table S4 and Table S5. Figure S39 supported that LD-DOX could effectively encapsulate and control release of PTX. Therefore, LD-DOX could be a versatile, efficient nano-platform for drug delivery. Ce6 as a dye-based photosensitizer was selected for encapsulation into LD-DOX as a model nanodrug for chemo-photodynamic combination anti-tumor therapy. Successful encapsulation of Ce6 was evidenced by the Ce6 characteristic absorbance peak (660 nm) of the resulting product in PBS (**Figure 2**a) or DMSO (Figure S40). With increasing the feeding amount of Ce6, the Ce6 loading in the LD-DOX NPs gradually increased, with the Ce6 encapsulation efficiency reaching the maximum of 74.3% at a DOX:Ce6 ratio of 1:1.5 (wt/wt) (Figure 2b and Table S4). Therefore, the NPs obtained at this ratio, with the Ce6 loading content of 10.0 wt%, were chosen for the further study and named as LD-DOX/Ce6. It is worth noting that compared with LD-DOX, the size of LD-DOX/Ce6 increased (Figure 2c), which might be due to the fact that Ce6 entered the hydrophobic core of the NPs, causing the expansion of the NPs core. The UV-vis absorbance spectra of the LD-DOX/Ce6, free DOX and free Ce6 were compared. As shown in Figure 2d, a characteristic peak corresponding to Ce6 was observed in LD-DOX/Ce6 but absent in LD-DOX, which further indicated a successful entrapment of Ce6. In addition, Figure 2e shows that the LD-DOX/Ce6 had similar photostability as free Ce6, and could well resist photobleaching under extended laser irradiation, indicating that it can be used as a good photosensitizer candidate for photodynamic therapy (PDT). Colloidal stability of the NPs solution has an important

influence on their *in vivo* distribution and accumulation at tumor sites.[22] As shown in Figure 2f, LD-DOX/Ce6 displayed negligible changes in both particle size and polydispersity index (PDI) after incubation in PBS for up to 48 h. Similar results were detected when it was incubated in PBS containing 10% fetal bovine serum (FBS) or the cell culture medium without FBS (Figure S41a and S41b). In addition, LD-DOX exhibited great stability under 4 °C storage conditions, and it was well re-dispersed in an aqueous solution after lyophilization (Figure S41c and S41d).

The drug release profiles of LD-DOX/Ce6 NPs were analyzed by the dialysis method. As shown in Figures 2g and 2h, after incubation in the absence of cathepsin B for 48 h, only 12% of DOX and 25% of Ce6 were released at pH 7.4, while in contrast, at pH 5.4, 82% of DOX and 66% of Ce6 were released. The release rates for both DOX and Ce6 were significantly increased in the presence of cathepsin B at pH 5.4, with about 78% of DOX and 63% of Ce6 released within 12 h. In addition, the degradation products were further characterized by HPLC and MALDI-TOF MS, which proved that the released DOX and Ce6 did not change in structure (Figure S42). DOX was rapidly released at pH 5.4 because the hydrazine linker between DOX and the linear-dendritic polymer is cleavable under acidic conditions. Upon release of DOX, the balance between hydrophilicity and lipophilicity in the NPs was damaged and the π-π interactions were weakened, resulting in the NPs disassembly to release the entrapped Ce6. In the meanwhile, the cathepsin B-sensitive GFLG tetrapeptide linker between the dendritic chains and the linear polymer backbone was specifically cleaved in the presence of cathepsin B to further facilitate disintegration of the nanostructures. As a result, the release rates of both DOX and Ce6 were accelerated to enhance therapeutic efficacy.

PDT kills cancer cells by cytotoxic reactive oxygen species (ROS) produced by photoactivated photosensitizers upon irradiation. In this work, the production yield of the singlet oxygen (SO), one type of ROS, from LD-DOX/Ce6 and free Ce6 upon irradiation with a 660-nm laser was investigated using the Singlet Oxygen Sensor Green (SOSG) as a probe. As shown in Figure S43a-e, the fluorescence intensity of SOSG remained at the base-line level in the control groups (free Ce6, LD-DOX/Ce6 NPs without laser irradiation, DOX with laser irradiation or LD-DOX with laser irradiation), while an irradiation time-dependent enhancement in the SOSG fluorescence intensity was observed in the LD-DOX/Ce6 solution upon irradiation (Figure 2i), which was similar to free Ce6 under the same irradiation condition (Figure S40c), suggesting that after irradiation, the LD-DOX/Ce6 NPs efficiently produced ROS at an equivalent level to free Ce6.

We investigated the cellular uptake of LD-DOX/Ce6 by detecting the fluorescence signals of Ce6 and DOX. The fluorescence intensities of free Ce6, free DOX and LD-DOX/Ce6 NPs were observed by confocal laser scanning microscopy (CLSM). As shown in **Figure 3**a for LD-DOX/Ce6 NPs, co-existence of strong fluorescence of DOX and Ce6 in the cells was observed. In addition, the fluorescence of free DOX was distributed in the nucleus, while under the same conditions the fluorescence from DOX in the LD-DOX/Ce6 NPs was mainly found in the cytoplasm, further indicating that intracellular distribution of the therapeutic agent DOX may be influenced by the LD-DOX/Ce6 delivery system (Figure S44). In addition, we further evaluated the uptake of LD-DOX/Ce6 by multicellular spheroids (MCSs). As shown in Figure S45, the fluorescence intensity of DOX and Ce6 in the MCSs increased with increasing the incubation time. After 6 h of incubation, a significant fluorescence distribution was observed in the MCSs at a depth of 60 μm (Figure 3b), indicating that the LD-DOX/Ce6 NPs have a good uptake and penetration capabilities the *in vitro* three-dimensional (3D) model mimicking 4T1 tumor tissues.

To determine the level of ROS produced in 4T1 cells under laser irradiation after internalization of the LD-DOX/Ce6, 4T1 cells were incubated with different Ce6-containing formulations and the intracellular ROS were detected with a fluorescent probe DCFH-DA. After DCFH-DA was internalized, intracellular ROS oxidized non-fluorescent DCFH to produce fluorescent DCF. The level of ROS in the cells was well correlated with the green fluorescence intensity of DCF. As shown in Figure 3c, the fluorescence intensity in the free Ce6 and NPs-treated groups was very weak without laser irradiation, as was similar to that of the control group. In contrast, after laser irradiation (660 nm, 10 mW $cm^{-2}$ for 30 s), there was an undetectable change in the fluorescence intensity in the control group, while significantly enhanced fluorescence was observed in the cells treated with LD-DOX/Ce6 or free Ce6. Flow cytometry analysis was used to quantify the level of intracellular ROS produced by different Ce6 formulations. Figure 3d revealed that after laser irradiation the Ce6- or LD-DOX/Ce6-treated cells produced a comparable level of ROS but much higher than the PBS-treated cells, which was consistent with the results shown in Figure 3c. These results indicated that photosensitizers significantly promoted ROS production in tumor cells only after the cells were irradiated by a 660 nm laser, thereby exerting their therapeutic effect. γH2A.X is an established marker of double-stranded DNA breaks and is widely used for detection of early DNA damage.[23] Previous studies have shown that both DOX and PDT can cause vital and irreversible damage to DNA. As shown in Figures 3e and 3f, compared with the control group,

each experimental group caused significant cellular DNA damage after treatment, indicating that both chemotherapy and PDT can damage cancer cells through DNA damage.

The *in vitro* anti-tumor effect of various formulations was examined with a CCK-8 assay kit. Cytotoxicity of free Ce6 in the darkness was shown in Figure S46a. Free Ce6 exhibited no obvious toxicity toward 4T1 cells even at a high concentration of Ce6 up to 30 μg $mL^{-1}$. In contrast, after laser irradiation (660 nm, 10 mW $cm^{-2}$) for 30 s, the concentration-dependent cytotoxicity to 4T1 cells was observed, showing a very low viability of 4T1 cells (less than 10%) at a Ce6 concentration of above 10 μg $mL^{-1}$. As the exposure time extended from 0.5 to 1 and 2 min, the $IC_{50}$ values of free Ce6 toward 4T1 cells gradually decreased from 6.94 to 4.06 and 1.56 μg $mL^{-1}$, respectively (Figure S46b). Furthermore, at a Ce6 concentration of 3 μg $mL^{-1}$, when the laser energy increased from 0 to 4.511 J $cm^{-2}$, the viability of 4T1 cells remarkably decreased from 100% to 5% (Figure S46c), indicating the cytotoxicity induced by laser irradiation was energy dependent. These results confirmed that Ce6, a photodynamic therapy agent, had potent cytotoxicity toward 4T1 cells after laser irradiation.

Subsequently, the *in vitro* anti-tumor efficacy of LD-DOX/Ce6 on 4T1 cells was investigated. POEGMA and low-generation glutamate dendrons showed no cytotoxicity to 4T1 cells, even at high concentrations (Figure s47a and b). And Figure 3g displayed a concentration-dependent inhibitory effect toward 4T1 cells treated with DOX, Ce6 with laser irradiation (Ce6+L), LD-DOX, LD-DOX/Ce6 and LD-DOX/Ce6 with laser irradiation (LD-DOX/Ce6 + L) at various DOX or Ce6 concentrations. The combination of chemotherapy (as a result of DOX release from LD-DOX/Ce6 NPs) and PDT (as a result of ROS generation from LD-DOX/Ce6 upon laser irradiation) was demonstrated to be more effective in tumor cell growth suppression than single chemotherapeutic treatment or PDT. The $IC_{50}$ values of LD-DOX/Ce6 + L, LD-DOX/Ce6, LD-DOX and Ce6 + L against 4T1 cells were calculated to be 0.14, 1.33, 2.01 and 6.94 μg $mL^{-1}$, respectively (Figure S47c). Free DOX usually has higher cytotoxicity than its prodrug counterparts due to its ability to rapidly enter cells by free diffusion, which results in a lower $IC_{50}$ value. However, it is noteworthy that the cytotoxicity of LD-DOX/Ce6 + L was comparable with free DOX ($IC_{50}$ = 0.14 μg $mL^{-1}$ for free DOX) due to the bi-modal therapeutic functions. In addition, we have analyzed the combination index (CI) of LD-DOX NPs and Ce6. The results showed that the CI value was less than 1, which further indicated that LD-DOX NPs and Ce6 synergistically inhibit the proliferation of 4T1 cells (Figure S48).

The effectiveness of the chemo-PDT combination treatment of 4T1 cells was further evaluated by quantifying the level of apoptosis by flow cytometry. Figures 3h and 3i

displayed the 4T1 cell populations in Q1, Q2, Q3 and Q4 zones, which represent dead cells, cells with late apoptosis, cells with early apoptosis and viable cells, respectively, after treatment with different formulations. Similar to the PBS-treated control group, continuous irradiation of 4T1 cells with 660 nm laser (10 mW $cm^{-2}$) for 30 s in the absence of formulations caused negligible apoptosis, indicating that laser irradiation did not cause obvious cell damage. As comparison, a high percentage of apoptotic cells (81.9% of cells with early and late apoptosis) was observed after the combination treatment (LD-DOX/Ce6 + L). This was in good agreement with the cytotoxicity result shown in Figure 3g, confirming the combined chemo-PDT of the LD-DOX/Ce6 NPs significantly improved the anti-tumor effect *in vitro*.

In order to further understand the molecular mechanisms of the combined effect of DOX and Ce6 in tumor suppression, RNA-seq was performed to compare the transcriptomics change of tumor cell samples after different treatments. The heat map showed the differentially expressed genes (DEGs) treated by control (treated with PBS), free DOX, Ce6 + L and LD-DOX/Ce6 + L (**Figure 4**a). These DEGs were mainly related to DNA damage repair (Brca1, Ercc1 Uvssa and Rpa2), apoptosis (CD44), Epithelial-Mesenchymal transition (MMP3, MEST, TGFB1, FOXC2, BMP1, Hmox1, and Hspb1), cell cycle (Ccne2, Erbb3, Ccnb2, and Ccnd1), and proliferation pathways (Isg15 and Btg2). The volcano plot also showed the genes related to DNA repair (Eid3, Prdm9 and Fancg) and cell cycle arrest (Ccne2) were upregulated, while the genes related to tumor growth (Dach1 and App), TGFβ pathway (Tgfb1) and Epithelial-Mesenchymal transition (Mmp9 and Stc1) were downregulated in LD-DOX/Ce6 + L group compared with control (Figure 4b). Gene ontology (GO) term enrichment analysis and KEGG enrichment analysis showed that compared with the control group, the genes up-regulated after LD-DOX/Ce6 + L treatment mainly involved DNA repair, DNA replication pathways (Figure 4c and 4d).

In addition, Gene Set Enrichment Analysis (GSEA) revealed a positive enrichment in the gene signatures for apoptosis (NES = 1.76, FDR = 0.04), DNA repair (NES = 1.75, FDR = 0.04), and cell cycle arrest (NES = 1.79, FDR = 0.03) in the LD-DOX/Ce6 + L group. DNA repair is a correcting response of the cell to DNA damage and alterations. Therefore, treatment with LD-DOX/Ce6 + L could directly induce cell death by causing DNA damage, blocking cell cycle as well as inducing cell apoptosis. A negative enrichment was found in the gene signatures for epithelial-mesenchymal transition (EMT, NES = -2.02, FDR = 0.0), angiogenesis (NES = -1.85, FDR = 5.79E-4), and TGFβ signaling (NES = -2.07, FDR = 0.0) in cells treated with LD-DOX/Ce6 + L comparing to those treated with the control (Figure 4e).

It has been documented that EMT and the TGFβ pathway are strongly associated with tumor cell migration and invasion,[24] thus these data suggested that the metastatic ability of cancer cells was significantly inhibited by combination treatment by LD-DOX/Ce6 + L.

Importantly, compared with cells treated with Ce6 + L or DOX alone, the combination treatment further suppressed the EMT pathway, the TGFβ pathway, angiogenesis and the hypoxia pathway (Figure S49a and S49b). It has been reported that hypoxia-inducible factor 1 (HIF1) is an important factor for promoting cancers development. The HIF1A pathway has been documented to be strongly associated with tumor metastasis, angiogenesis, poor patient prognosis as well as tumor resistance for chemotherapy.[25] The above data suggested the combination treatment significantly inhibited tumor metastasis compared with DOX or Ce6 + L alone. Meanwhile, the combination treatment upregulated the DNA repair pathway (NES = 1.53, FDR = 0.01 and NES = 1.82, FDR = 0.04 in comparison with free DXO and Ce6+L, respectively), which indicated the combination treatment induced more severe DNA damage (Figure S49a). In addition, the combination treatment directly induced apoptosis at a higher level compared with those received the Ce6 + L treatment (NES = 2.03, FDR = 0.001) (Figure S49a). Therefore, the combination treatment could not only suppress tumor growth, but also significantly reduced tumor metastasis compared with treatments with DOX or Ce6 + L.

The DOX treatment induced apoptosis (NES = 1.49, FDR = 0.03), and inhibited the Myc targets pathway (NES = -2.62, FDR = 0.0) and the HIF1A pathway (NES = -1.68, FDR = 0.12) compared with the control group (Figure S49c), which indicate the DOX treatment promoted cancer cells death and suppressed tumor growth and tumor metastasis. Besides suppression of the cell proliferation pathway (NES = -1.95, FDR = 0.008), the Ce6 + L treatment also inhibited the HIF1A pathway (NES = -1.82, FDR = 0.02) and the NF-κB pathway (NES = -2.36, FDR = 0.0) compared with the control group (Figure S49d). The NFκB pathway is extensively involved in cancer development and progression, and it mediates tumor cell proliferation, survival, and angiogenesis through regulating the expression of TNFA, IL6, BCL2, and VEGF.[26] Therefore, treatment with either DOX or Ce6 + L could suppress tumor growth and metastasis.

Consistent with bioinformatics analysis, the western blots supported that after treatment with free DOX, Ce6 + L or LD-DOX/Ce6 + L, the apoptosis-related proteins, including Bax, cleaved caspase-3 and cleaved PARP, were significantly up-regulated (Figure 4f and Figure S50). In addition, expression of γH2A.X, a DNA damage-associated marker, was also significantly enhanced in cells after treatment with free DOX, Ce6 + L, or LD-DOX/Ce6 + L (Figure 4f and Figure S50).

Encouraged by the excellent anti-tumor effect of LD-DOX/Ce6 *in vitro*, its biocompatibility was evaluated through acute toxicity tests. As shown in Figure S51, free DOX displayed obvious dose-dependent toxicity, and injection of DOX at high doses into mice (10 mg $kg^{-1}$ and 15 mg $kg^{-1}$) resulted in severe weight loss and even death. In contrast, mice in the LD-DOX- and LD-DOX/Ce6-treated groups survived at a dose equivalent to 30 mg DOX $kg^{-1}$. Furthermore, H&E staining results of the mice treated with DOX at 10 mg $kg^{-1}$ revealed that the liver and heart exhibited distinct pathological changes (Figure S52), which was consistent with their severe weight loss. In addition, blood routine and biochemical test results showed that ALT, AST, RBC, and PLT of the DOX-treated group were significantly different from those in the control group (Figure S53 and S54), further indicating that DOX had serious side effects. However, these blood test indexes in the LD-DOX- and LD-DOX/Ce6-treated groups were not significantly different from those in the control group at the equivalent dose of DOX (Figure S53 and S54), which demonstrated that the systemic toxicity of DOX was significantly reduced, and both LD-DOX and LD-DOX/Ce6 had great biocompatibility. The *in vivo* skin photosensitivity of Ce6 and LD-DOX/Ce6 NPs were also assessed. As shown in Figure S55, the mice treated with Ce6 suffered severe skin damage after exposure to a 660 nm laser. The H&E sections displayed severe necrosis in the skin. In contrast, mice treated with LD-DOX/Ce6 only exhibited slight edema after laser irradiation, and after 5 days, no significant difference in the H&E sections was found between the LD-DOX/Ce6-treated group and the control group. Overall, these results strongly supported in vivo biocompatibility and biosafety of LD-DOX/Ce6, laying a solid foundation for its application as chemical-photodynamic combination therapy in vivo.

The PEGylated nanoscale drug delivery system has the potential to significantly improve the pharmacokinetics of small molecule drugs, thereby enhancing their therapeutic effects.[27] After female BALB/c mice were (i.v.) administered with free Ce6 and LD-DOX/Ce6 at an equivalent Ce6 dose of 5.0 mg $kg^{-1}$, respectively, the blood samples were collected at different time points after injection, and the Ce6 concentration in the blood was determined by measuring the Ce6 fluorescence. As shown in **Figure 5**a, no Ce6 fluorescence signal was detected at 8 h post injection, suggesting that free Ce6 was eliminated from the blood circulation system. As comparison, the blood retention time of Ce6 was significantly prolonged in LD-DOX/Ce6, and the fluorescent signal of Ce6 was still detectable in the blood (1.17 μg $mL^{-1}$) at 12 h post injection.

The pharmacokinetic parameters from the non-compartmental analysis were summarized in Table S6. The elimination half-life time ($t_{1/2}$) of LD-DOX/Ce6 was 13.6 h, which was 8.5

times that of free Ce6 (1.6 h). In addition, other pharmacokinetic parameters of Ce6 in LD-DOX/Ce6 NPs were also significantly different from free Ce6: a longer mean residence time (MRT(0-∞)) (18.4 vs 1.5 h), a higher area under the curve (AUC(0-∞)) (4184.2 vs 493.0 μg $mL^{-1}$ min) and a significantly lower total clearance (CL) (0.024 vs 0.203 (μg $mL^{-1}$ $min^{-1}$)). These results indicated that the chemo-PDT combination system significantly increased the *in vivo* circulation time of Ce6, which may be due to the excellent stability of the NPs, as well as the protective layer of polyOEG on the periphery of the NPs.

The prolonged blood circulation time of LD-DOX/Ce6 prompted us to further investigate the targeting ability of NPs in an orthotopic 4T1 breast tumor model in BALB/c mice. As shown in Figure 5b, the LD-DOX/Ce6 NPs showed excellent targeting in orthotopic 4T1 breast tumor model, and a large amount of LD-DOX/Ce6 accumulated in the primary tumor after i.v. administration. In addition, the results of the window model also confirmed the gradual increase in fluorescence intensity at orthotopic 4T1 breast tumor within 6 h of administration, indicating that the NPs can effectively enrich and diffuse in the tumor site (Figure 5c).

Furthermore, the more detailed biodistribution of LD-DOX/Ce6 in tumor-bearing mice was revealed by *ex vivo* fluorescence imaging. Tumor-bearing mice were i.v. injected with free Ce6 or LD-DOX/Ce6 and then sacrificed at predetermined time points post-injection, and major organs and tumors were collected for *ex vivo* fluorescence imaging. Figure 5d showed representative fluorescence images of major organs extracted from the mice 24 h after i.v. injection with LD-DOX/Ce6. Compared with free Ce6, the fluorescence intensity of the tumor site in mice after LD-DOX/Ce6 administration increased significantly, indicating that it can effectively target the tumor site. Specifically, as shown in Figure S56, the Ce6 fluorescence in both free Ce6 and LD-DOX/Ce6-treated groups was rapidly distributed to the liver, lung, kidney and tumor, but mainly concentrated in the liver after 1 h of administration. The Ce6 fluorescence in the liver, lung and kidney of the free Ce6-treated group gradually decreased with time, and after 12 h of administration very weak Ce6 fluorescence was observed in the liver. At the same time, the Ce6 fluorescence of the tumor site was at a low level at each time point. As comparison, within 24 h of administration, strong Ce6 fluorescence signals in LD-DOX/Ce6-treated group was observed the liver, lung, kidney and tumor, and significant increase Ce6 fluorescence was observed at the tumor site. It was worth noting that the accumulation of LD-DOX/Ce6 at the liver was significantly reduced at 1 h post injection in comparison with free Ce6, probably due to the presence of the POEGMA-based polymer shell to reduce uptake by the macrophage and reticuloendothelial system. These observations were

confirmed from semi-quantitative analysis of the fluorescence intensity at tumor and major organs, as shown in Figures S57a and S57b. The semi-quantitative analysis demonstrated that the retention time of LD-DOX/Ce6 in mice was significantly prolonged, and the strong fluorescence signals at the tumor site indicated that NPs may be effectively enriched at the tumor site through the EPR effect. In addition, compared to free Ce6, the accumulation of LD-DOX/Ce6 at the tumor site gradually increased with time, with the average fluorescence peaked at 24 h and then maintained a relatively high level up to 72 h (Figure S57c). These results were consistent with the pharmacokinetic data shown in Figure 5a, indicating that LD-DOX/Ce6 effectively prolonged the circulation time of the therapeutic agent Ce6 in the body, improved its biodistribution, and increased its accumulation at the tumor site. Bright red fluorescence of Ce6 was observed in the frozen sections of the tumor tissue from the LD-DOX/Ce6-administered group at different time points (Figure 5e). In contrast, Ce6 fluorescence was very weak in the tumor tissue of the free Ce6-treated mice (Figure S58). These results were consistent with the *ex vivo* fluorescence images shown in Figure 5d, further indicating that LD-DOX/Ce6 were capable of efficiently delivering Ce6 to the tumor site as due to the EPR effect.

The *in vivo* anti-tumor efficacy of LD-DOX/Ce6 was first evaluated using the subcutaneous 4T1 tumor model (Figure 5f). The tumor volume was monitored and the change in the tumor volume of different treatment groups was shown in Figure 5g. For the group with laser irradiation alone, the tumor volume rapidly increased, the growth trend and relative tumor volume were very similar to that of the saline group, indicating that laser irradiation had no inhibitory effect on tumor growth under the irradiation condition employed in this study. Compared to the single therapy (Group 3 (G3: Ce6 + L) for PDT or Group 4 (free DOX) for chemotherapy), LD-DOX/Ce6 without laser irradiation (Groups 5 and 6) showed slightly better tumor-inhibitory effects, while LD-DOX/Ce6 with laser irradiation (Groups 7 and 8) displayed the strongest inhibitory efficacy with a marginal change in the tumor volume up to 21 days, suggesting that the combination of chemotherapy and PDT significantly improved the anti-tumor efficacy.

It was worth noting that as the dose of the therapeutic agent increased, the anti-tumor effect was enhanced accordingly. However, at a sufficiently high concentration of 8 mg $kg^{-1}$ (Group 9), although free DOX showed a remarkable tumor suppressing effect, the weight of these mice was reduced below 80% of their initial weight after 13 days of treatment, and the mice died before the end of the experiment, indicating the severe systemic toxicity of free DOX (Figure 5g and 5h). In contrast, treatment of the mice with LD-DOX/Ce6 containing an

equivalent DOX concentration of 8 mg $kg^{-1}$ with laser irradiation (Group 8) did not induce a significant change in the body weight during the period of 21 days tested (Figure 5h). These results indicated that LD-DOX/Ce6 with laser irradiation effectively enhanced the anti-tumor effect and reduced the unwanted side effects associated with free DOX, which was attributed to the significantly improved *in vivo* distribution and accumulation of DOX at the tumor site by the NPs. At the end of the experiment, tumors of each treatment group were stripped and photographed (Figure S59a). The tumors were weighed and the growth inhibition rates in relation to the different treatments were calculated (Figure 5i). A wide range of anti-tumor efficacies were found in different groups compared to the saline group (Group 1). The tumor growth inhibition (TGI) value for Groups 2–8 was 3.3%, 19.5%, 29.3%, 35.2%, 39.7%, 63.2%, and 76.2%, respectively (Figure S59b). Among those treatment groups, LD-DOX/Ce6 with laser irradiation (8 mg DOX $kg^{-1}$, 8.9 mg Ce6 $kg^{-1}$) resulted in the lowest average tumor weight (253 ± 47 mg) and the highest TGI (76.2%), which was consistent with the trend of the tumor volume change (Figure 5f). The anti-tumor effect of the NPs was further revealed using Hematoxylin–eosin (H&E) staining. As shown in Figure S60, different degrees of structural damage were observed in the tumor sections of each treatment group compared to the control group. Among them, the tumor sections from mice treated with LD-DOX/Ce6 + L (8 mg DOX $kg^{-1}$, 8.9 mg Ce6 $kg^{-1}$) displayed the highest degree of morphological damage and tumor cell necrosis. In order to reveal the anti-tumor mechanism of LD-DOX/Ce6, IHC analysis of tumors in each group of mice was carried out. As shown in Figure S60, tumor microvascular staining displayed that the vascular density of the tumor site for Group 8 treated with the LD-DOX/Ce6 with laser irradiation (8 mg DOX $kg^{-1}$, 8.9 mg Ce6 $kg^{-1}$) was significantly reduced compared with the other treatment groups, indicating that the combination chemo-photodynamic therapy effectively inhibited tumor angiogenesis. The expression of Ki-67 in the tumor sections through Ki-67 tumor staining was significantly decreased for Group 8, suggesting that tumor cell proliferation was significantly inhibited after the chemo-PDT treatment. The TUNEL immunohistochemistry was further used to confirm apoptosis of tumor cells. Each treatment group exhibited different degrees of apoptosis compared with the saline group (Figure S60). Among them, treatment with Group 8 resulted in the highest number of apoptotic tumor cells, demonstrating its strongest ability to induce tumor cell apoptosis, which was consistent with the results of H&E staining. The *in vivo* data indicated that this chemo-PDT combination treatment demonstrated a better therapeutic efficacy than treatment by DOX or laser irradiation alone, and exerted its anti-tumor effect by reducing angiogenesis, inhibiting tumor cell proliferation, and inducing apoptosis. In addition, the

toxicology of various formulations was also determined by the H&E assay. Compared to the control organs (including heart, liver, spleen, kidneys, and lungs), no obvious abnormalities were found in the organ sections after various treatments (Groups 2 to 8) (Figure S61), demonstrating excellent biosafety of these formulations, including LD-DOX/Ce6.

Furthermore, we evaluated the therapeutic effect of the LD-DOX/Ce6 on breast cancer orthotopic models. As expected, compared to the single therapy, the combination treatment group (LD-DOX/Ce6 + L) showed the best anti-tumor treatment effect (Figure 5j), and the survival time of the mice was significantly prolonged (Figure 5k). It is worth noting that breast cancer, especially breast cancer in situ, is easy to metastasize to the lungs. Therefore, we detected lung tumor metastasis of mice in each treatment group by CT imaging and H&E histology analysis (Figures 5l and 5m). The 3D model of the lungs shown in Figure 5m demonstrated that after 21 days of treatment, a large number of tumor metastases were detected in the lungs of the mice treated with saline and Ce6+L. In contrast, although single chemotherapy groups (DOX, LD-DOX and LD-DOX/Ce6) could attenuate metastasis formation in lung, they still could not completely limit tumor metastasis. Markedly, no visible tumor metastases were found in mice treated with LD-DOX/Ce6 + L. The tumor metastasis was further confirmed by the H&E staining and number count of metastatic tumor nodules in lung lobe sections from mice at the endpoint of various treatments (Figures 5l and 5m). Obvious metastatic tumor nodules could be observed in the saline and Ce6 + L groups (indicated by the yellow arrows), while the LD-DOX/Ce6 + L-treated group showed normal appearance similar to normal lung tissue, which was consistent with the long-term survival after treatment. The above results indicated that the combination of chemotherapy and PDT not only inhibited the growth rate of tumors, but also significantly prolonged the survival time of mice by inhibiting the lung metastasis of tumors.

**3. Conclusion**

In summary, we have successfully prepared a DOX-loaded polymer prodrug based on a linear-dendritic polymer by two-step RAFT polymerization, and then encapsulated Ce6 to obtain the enzyme and pH-sensitive antitumor prodrug-based NPs (LD-DOX/Ce6). The NPs have been demonstrated to prolong their circulation time and to enhance their accumulation at tumor sites through the EPR effect. In the tumor microenvironment with overexpressed cathepsin B and a weakly acidic condition, the nanostructure of the NPs was disintegrated to simultaneously release DOX and Ce6, and Ce6 was further exposed to laser irradiation to generate ROS, resulting in a significantly improved synergistic therapeutic efficacy and reduced systemic toxicity, improved synergistic therapeutic efficacy through regulating cell

apoptosis, DNA repair and cell cycle arrest, and inhibited tumor metastasis by suppressed EMT pathway, the TGFβ pathway, angiogenesis and the hypoxia pathway. Our results demonstrate that the linear-dendritic based polymeric prodrug may be explored as a new class of multifunctional drug carriers for incorporating multiple therapeutic agents for multi-modal therapy against cancer.

## 4. Experimental Section

Materials, methods, synthetic procedures, cell and animal experiments, other data, and associated references are available in the Supporting Information. All animal operation procedures were carried out with the approval of the ethics committee of West China Hospital, Sichuan University (No. 2018148A and 2018150A).

## 5. Statistical analysis

All numeric data are expressed as mean ± standard deviation (SD), unless otherwise indicated. Differences between groups were assessed using Student's t test. Statistical analysis was performed using GraphPad Prism 7.0. *P* values of less than 0.05 were considered significant; $*P < 0.05$, $**P < 0.01$, $***P < 0.001$ and $****P < 0.0001$.

## Supporting Information

Supporting Information is available from the Wiley Online Library or from the author.

## Acknowledgements

This work was financially supported by National Natural Science Foundation of China (52073193, 51873120 and 81621003), 1·3·5 Project for Disciplines of Excellence, West China Hospital, Sichuan University (ZYJC21013, ZYGD20007, ZYJC18011 and ZYGD18011), Research Funds in West China Hospital of Sichuan University (19HXBH057, 2020HXBH094), and China Postdoctoral Science Foundation (2021M692255), China National Postdoctoral Program for Innovation Talents (BX20200229). M. Kopytynski was supported by the NIHR Imperial Biomedical Research Centre (BRC). The authors thank Sisi Wu, Zhiiqan Li, Yu Ding, Xuemei Chen, Li Fu, Huaiqiang Sun, Shenglan You, Lei Wu and Qing Yang (Research Core Facility, West China Hospital, Sichuan University) for their help in cell studies and histological studies. The authors would like to thank Li Li, Fei Chen, Chunjuan Bao, and Yang Deng from Laboratory of Pathology, West China Hospital, Sichuan University for helping with processing the historical sections and staining. The authors thank Ping Liao (Department of Anesthesiology of West China Hospital, Sichuan University, Chengdu, Sichuan, China) for imaging analysis. The authors would also like to thank Xue Li

and Qiaorong Huang (Laboratory of Stem Cell Biology, West China Hospital, Sichuan University) for their help with flow cytometry.

## Conflict of Interest

The authors declare no conflict of interest.

Received: ((will be filled in by the editorial staff))
Revised: ((will be filled in by the editorial staff))
Published online: ((will be filled in by the editorial staff))

## References

[1] a) X. Tian, S. Angioletti-Uberti, G. Battaglia, *Sci. Adv.* **2020**, *6*, eaat0919; b) Q. Zhou, S. Shao, J. Wang, C. Xu, J. Xiang, Y. Piao, Z. Zhou, Q. Yu, J. Tang, X. Liu, Z. Gan, R. Mo, Z. Gu, Y. Shen, *Nat. Nanotechnol.* **2019**, *14*, 799-809; c) Y. Dong, Y. Tu, K. Wang, C. Xu, Y. Yuan, J. Wang, *Angew. Chem. Int. Ed.* **2020**, *59*, 7168-7172; d) R. van der Meel, E. Sulheim, Y. Shi, F. Kiessling, W. J. M. Mulder, T. Lammers, *Nat. Nanotechnol.* **2019**, *14*, 1007-1017; e) Z. Duan, Q. Luo, X. Dai, X. Li, L. Gu, H. Zhu, X. Tian, H. Zhang, Q. Gong, Z. Gu, K. Luo, *Adv. Mater.* **2021**, *33*, e2104594; f) J. Gao, J. Zhan, Z. Yang, *Adv. Mater.* **2020**, *32*, e1805798.

[2] a) S. Ahmadi, N. Rabiee, M. Bagherzadeh, F. Elmi, Y. Fatahi, F. Farjadian, N. Baheiraei, B. Nasseri, M. Rabiee, N. T. Dastjerd, A. Valibeik, M. Karimi, M. R. Hamblin, *Nano today* **2020**, *34*, 100914; b) W. H. Chen, G. F. Luo, X. Z. Zhang, *Adv. Mater.* **2018**, *31*, 1802725; c) Z. Tang, Y. Liu, M. He, W. Bu, *Angew. Chem. Int. Ed.* **2019**, *58*, 946-956; d) J. Liu, Q. Chen, L. Feng, Z. Liu, *Nano today* **2018**, *21*, 55-73; e) C. Chen, H. Ou, R. Liu, D. Ding, *Adv. Mater.* **2020**, *32*, e1806331; (f) H. Cai, Y. Xiang, Y. Zeng, Z. Li, X. Zheng, Q. Luo, H. Zhu, Q. Gong, Z. Gu, Y. Liu, H. Zhang, K. Luo, *Acta Pharm. Sin. B* **2021**, *11*, 544-559.

[3] a) H. Sun, C. P. Kabb, M. B. Sims, B. S. Sumerlin, *Prog. Polym. Sci.* **2019**, *89*, 61-75; b) G. Polymeropoulos, G. Zapsas, K. Ntetsikas, P. Bilalis, Y. Gnanou, N. Hadjichristidis, *Macromolecules* **2017**, *50*, 1253-1290; c) Z. Wang, Y. Ju, Z. Ali, H. Yin, F. Sheng, J. Lin, B. Wang, Y. Hou, *Nat. Commun.* **2019**, *10*, 4418.

[4] a) O. S. Fenton, K. N. Olafson, P. S. Pillai, M. J. Mitchell, R. Langer, *Adv. Mater.* **2018**, *30*, 1705328; b) X. Liu, W. Lin, D. Astruc, H. Gu, *Prog. Polym. Sci.* **2019**, *96*, 43-105; c) H. Sun, F. M. Haque, Y. Zhang, A. Commisso, M. A. Mohamed, M. Tsianou, H. Cui, S. M. Grayson, C. Cheng, *Angew. Chem. Int. Ed.* **2019**, *131*, 10682-10686; d) N. Li, Z. Duan, L. Wang, C. Guo, H. Zhang, Z. Gu, Q. Gong, K. Luo, *Macromol. Rapid Commun.* **2021**, *42*, e2100111; e) X. Zheng, D. Pan, X. Chen, L. Wu, M. Chen, W. Wang, H. Zhang, Q. Gong, Z. Gu, K. Luo, *Adv. Sci.* **2021**, *8*, e2102741; f) Y. Wang, N. Gong, C. Ma, Y. Zhang, H. Tan, G. Qing, J. Zhang, Y. Wang, J. Wang, S. Chen, X. L. Li, Q. Ni, Y. Yuan, Y. Gan, J. Chen, F. Li, J. Zhang, C. Ou, Y. Zhao, X. Liu, X. Liang, *Nat. Commun.* **2021**, *12*, 4964; g) Q. Luo, Z. Duan, X. Li, L. Gu, H. Zhu, X. Tian, H. Zhang, Q. Gong, Z. Gu, K. Luo. *Adv. Func. Mater.* **2021,** DOI: 10.1002/adfm.202110408.

[5] a) S. Mignani, J. Rodrigues, H. Tomas, M. Zablocka, X. Shi, A.-M. Caminade, J.-P. Majoral, *Chem. Soc. Rev.* **2018**, *47*, 514-532; b) C. Gao, D. Yan, *Prog. Polym. Sci.* **2004**, *29*, 183-275; c) A. B. Cook, S. Perrier, *Adv. Funct. Mater.* **2019**, *30*, 1901001; d) H. Li, J. Sun, H. Zhu, H. Wu, H. Zhang, Z. Gu, K. Luo, WIREs *Nanomed. Nanobi.* **2020**, *13*; e) C. Song, M. Shen, J. Rodrigues, S. Mignani, J.-P. Majoral, X. Shi, Coordin. *Chem. Rev.* **2020**, *421*, 213463; f) A. Mtibe, M. P. Motloung, J. Bandyopadhyay, S. S. Ray, *Macromol. Rapid Commun*. **2021**, *42*, e2100130.

[6] a) X. Yan, Y. Yang, Y. Sun, *J. Phys.: Conf. Ser.* **2021**, *1948*, 012205; b) R. I. Castro, O. Forero-Doria, L. Guzman, *An. Acad. Bras. Cienc.* **2018**, *90*, 2331-2346.

[7] a) R. Bruni, P. Possenti, C. Bordignon, M. Li, S. Ordanini, P. Messa, M. P. Rastaldi, F. Cellesi, *J. Control. Release* **2017**, *255*, 94-107; b) B. Du, X. Jiang, A. Das, Q. Zhou, M. Yu, R. Jin, J. Zheng, *Nat. Nanotechnol.* **2017**, *12*, 1096-1102; c) S. Svenson, *Chem. Soc. Rev.* **2015**, *44*, 4131-4144; d) M. Elsabahy, K. L. Wooley, *Chem. Soc. Rev.* **2012**, *41*, 2545-2561; e) Q. Sun, M. Radosz, Y. Shen, *J. Control. Release* **2012**, *164*, 156-169.

[8] a) F. Wurm, H. Frey, *Prog. Polym. Sci.* **2011**, *36*, 1-52; b) C. Shi, D. Guo, K. Xiao, X. Wang, L. Wang, J. Luo, *Nat. Commun.* **2015**, *6*, 7449.

[9] O. C. J. Andrén, Y. Zhang, P. Lundberg, C. J. Hawker, A. M. Nyström, M. Malkoch, *Chem. Mater.* **2017**, *29*, 3891-3898.

[10] a) aI. Gitsov, J. Hamzik, J. Ryan, A. Simonyan, J. P. Nakas, S. Omori, A. Krastanov, T. Cohen, S. W. Tanenbaum, *Biomacromolecules* **2008**, *9*, 804-811; b) I. Gitsov, L. Wang, N. Vladimirov, A. Simonyan, D. J. Kiemle, A. Schutz, *Biomacromolecules* **2014**, *15*, 4082-4095; c) Z. Zhou, X. Ma, E. Jin, J. Tang, M. Sui, Y. Shen, E. A. Van Kirk, W. J. Murdoch, M. Radosz, *Biomaterials* **2013**, *34*, 5722-5735.

[11] E. Blasco, M. Pinol, L. Oriol, *Macromol. Rapid. Commun.* **2014**, *35*, 1090-1115.

[12] a) J. Luo, K. Xiao, Y. Li, J. S. Lee, L. Shi, Y.-H. Tan, L. Xing, R. Holland Cheng, G.-Y. Liu, K. S. Lam, *Bioconjugate Chem.* **2010**, *21*, 1216-1224; b) S. Mejlsøe, A. Kakkar, *Molecules* **2020**, *25*, 3995.

[13] a) P. Chytil, E. Koziolova, O. Janouskova, L. Kostka, K. Ulbrich, T. Etrych, *Macromol. Biosci.* **2015**, *15*, 839-850; b) I. Ekladious, Y. L. Colson, M. W. Grinstaff, *Nat. Rev. Drug Discov.* **2019**, *18*, 273-294; c) C. Boyer, V. Bulmus, T. P. Davis, V. Ladmiral, J. Liu, S. Perrier, *Chem. Rev.* **2009**, *109*, 5402-5436.

[14] a) F. Du, S. Bobbala, S. Yi, E. A. Scott, *J. Control. Release* **2018**, *282*, 90-100; b) S. Wang, G. Yu, Z. Wang, O. Jacobson, R. Tian, L. S. Lin, F. Zhang, J. Wang, X. Chen, *Adv. Mater.* **2018**, *30*, 1803926.

[15] Y. Qi, A. Simakova, N. J. Ganson, X. Li, K. M. Luginbuhl, I. Ozer, W. Liu, M. S. Hershfield, K. Matyjaszewski, A. Chilkoti, *Nat. Biomed. Eng.* **2016**, *1*, 0002.

[16] B. M. Cooper, J. Iegre, D. H. O' Donovan, M. Ölwegård Halvarsson, D. R. Spring, *Chem. Soc. Rev.* **2021**, *50*, 1480-1494.

[17] a) D. Pan, X. Zheng, Q. Zhang, Z. Li, Z. Duan, W. Zheng, M. Gong, H. Zhu, H. Zhang, Q. Gong, Z. Gu, K. Luo, *Adv. Mater.* **2020**, *32*, e1907490; b) D. Pan, X. Zheng, M. Chen, Q. Zhang, Z. Li, Z. Duan, Q. Gong, Z. Gu, H. Zhang, K. Luo, *J. Mater. Sci. Technol.* **2021**, *63*, 115-123.

[18] a) aB. S. Parker, D. R. Ciocca, B. N. Bidwell, F. E. Gago, M. A. Fanelli, J. George, J. L. Slavin, A. Moller, R. Steel, N. Pouliot, B. L. Eckhardt, M. A. Henderson, R. L. *Anderson, J. Pathol.* **2008**, *214*, 337-346; b) J. H. Ryu, J. H. Na, H. K. Ko, D. G. You, S. Park, E. Jun, H. J. Yeom, D. H. Seo, J. H. Park, S. Y. Jeong, I.-S. Kim, B.-S. Kim, I. C. Kwon, K. Choi, K. Kim, *Biomaterials* **2014**, *35*, 2302-2311.

[19] J. Mu, J. Lin, P. Huang, X. Chen, *Chem. Soc. Rev.* **2018**, *47*, 5554-5573.

[20] a) Y. Gao, Y. Chen, X. Ji, X. He, Q. Yin, Z. Zhang, J. Shi, Y. Li, *ACS Nano* **2011**, *5*, 9788-9798; b) T. Wang, D. Wang, H. Yu, M. Wang, J. Liu, B. Feng, F. Zhou, Q. Yin, Z. Zhang, Y. Huang, Y. Li, *ACS Nano* **2016**, *10*, 3496-3508.

[21] H. Zhang, *Methods Mol. Biol.* **2017**, *1522*, 17-22.

[22] J. H. Park, S. Lee, J.-H. Kim, K. Park, K. Kim, I. C. Kwon, *Prog. Polym. Sci.* **2008**, *33*, 113-137.

[23] a) L. Wang, W. Jiang, L. Xiao, H. Li, Z. Chen, Y. Liu, J. Dou, S. Li, Q. Wang, W. Han, Y. Wang, H. Liu, ACS Nano 2020, 14, 8459-8472; b) D. Zhong, H. Wu, Y. Wu, Y. Li, J. Yang, Q. Gong, K. Luo, Z. Gu, *J. Control. Release* **2021**, *329*, 1210-1221.

[24] I. Fabregat, J. Fernando, J. Mainez, P. Sancho, *Curr. Pharm. Design* **2014**, *20*, 2934-2947.

[25] G. N. Masoud, W. Li, *Acta pharm. Sin. B* **2015**, *5*, 378-389.

[26] L. Xia, S. Tan, Y. Zhou, J. Lin, H. Wang, L. Oyang, Y. Tian, L. Liu, M. Su, H. Wang, D. Cao, Q. Liao, *Onco Targets Ther.* **2018**, *11*, 2063-2073.

[27] a) J. S. Suk, Q. Xu, N. Kim, J. Hanes, L. M. Ensign, *Adv.Drug Deliver. Rev.* **2016**, *99*, 28-51; b) Y. Wu, F. Li, X. Zhang, Z. Li, Q. Zhang, W. Wang, D. Pan, X. Zheng, Z. Gu, H. Zhang, Q. Gong, K. Luo, *Carbohyd. Polym.* **2021**, *255*, 117490; c) C. Yang, X. Pang, W. Chen, X. Wang, G. Lin, C. Chu, X. Zhang, X. Deng, X. Chen, G. Liu, *Sci. Bull.* **2019**, *64*, 705-714; d) P. Zhang, Y. Zhang, X. Ding, W. Shen, M. Li, E. Wagner, C. Xiao, X. Chen, *Adv. Mater.* **2020**, *32*, e2000013.

## Figures

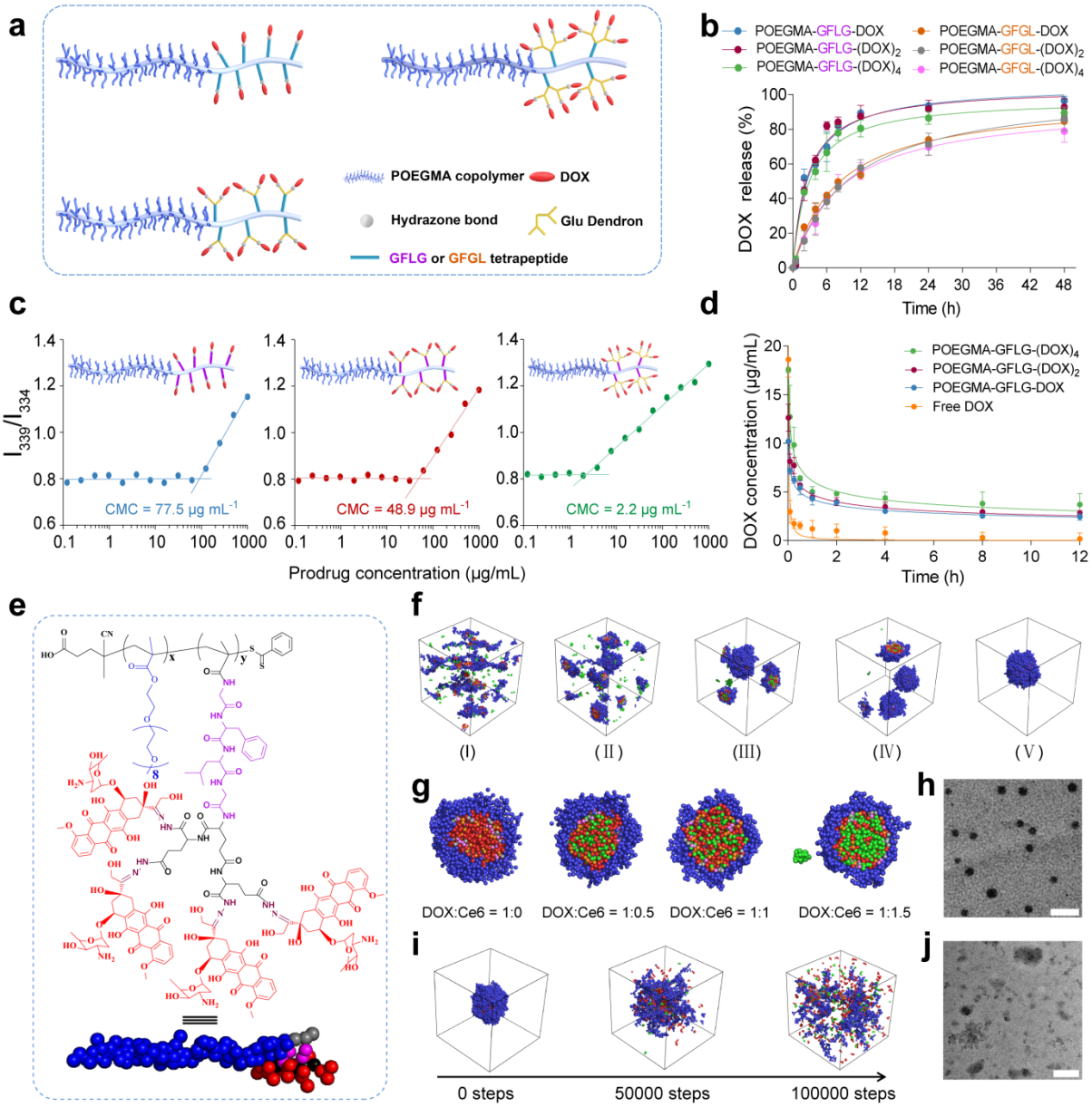



**Figure 1.** Physicochemical characterization and dissipative particle dynamics (DPD) simulation of prodrugs POEGMA-GFLG-$(DOX)_x$ and POEGMA-GFGL-$(DOX)_x$ (x = 1, 2 or 4). (a) Schematic design of the polymer prodrug structure used for comparison in this study. (b) DOX-release profiles of POEGMA-GFLG-$(DOX)_x$ and POEGMA-GFGL-$(DOX)_x$ in the presence of cathepsin B at pH 5.4. (c) Measurements of critical micelle concentration (CMC) of POEGMA-GFLG-DOX, POEGMA-GFLG-$(DOX)_2$ and POEGMA-GFLG-$(DOX)_4$ (from left to right) using pyrene as a fluorescence probe. (d) Plasma concentration profiles of free DOX, POEGMA-GFLG-DOX, POEGMA-GFLG-$(DOX)_2$ and POEGMA-GFLG-$(DOX)_4$ after an i.v. injection in mice. (e) Chemical structure and coarse-grained model of POEGMA-GFLG-$(DOX)_4$. (f) The modelling process of nanoparticle formation by POEGMA-GFLG-$(DOX)_4$ and Ce6 (green beads) loading in water. The DPD simulations were performed for 200,000 time steps with an integration time step of 0.02. (g) Formation of LD-DOX/Ce6 NPs at different feeding weight

ratios of Ce6 to DOX. (h) TEM images of LD-DOX/Ce6, scale bar = 50 nm. (i) Dynamic process of drug release from LD-DOX/Ce6 upon the simultaneous breakage of the hydrazone bond and GFLG, and 100,000 time steps were used to analyze the drug release process in protonation conditions. (j) TEM image of LD-DOX/Ce6 after incubation in deionized water at pH 5.4 for 24 h, scale bar = 200 nm.

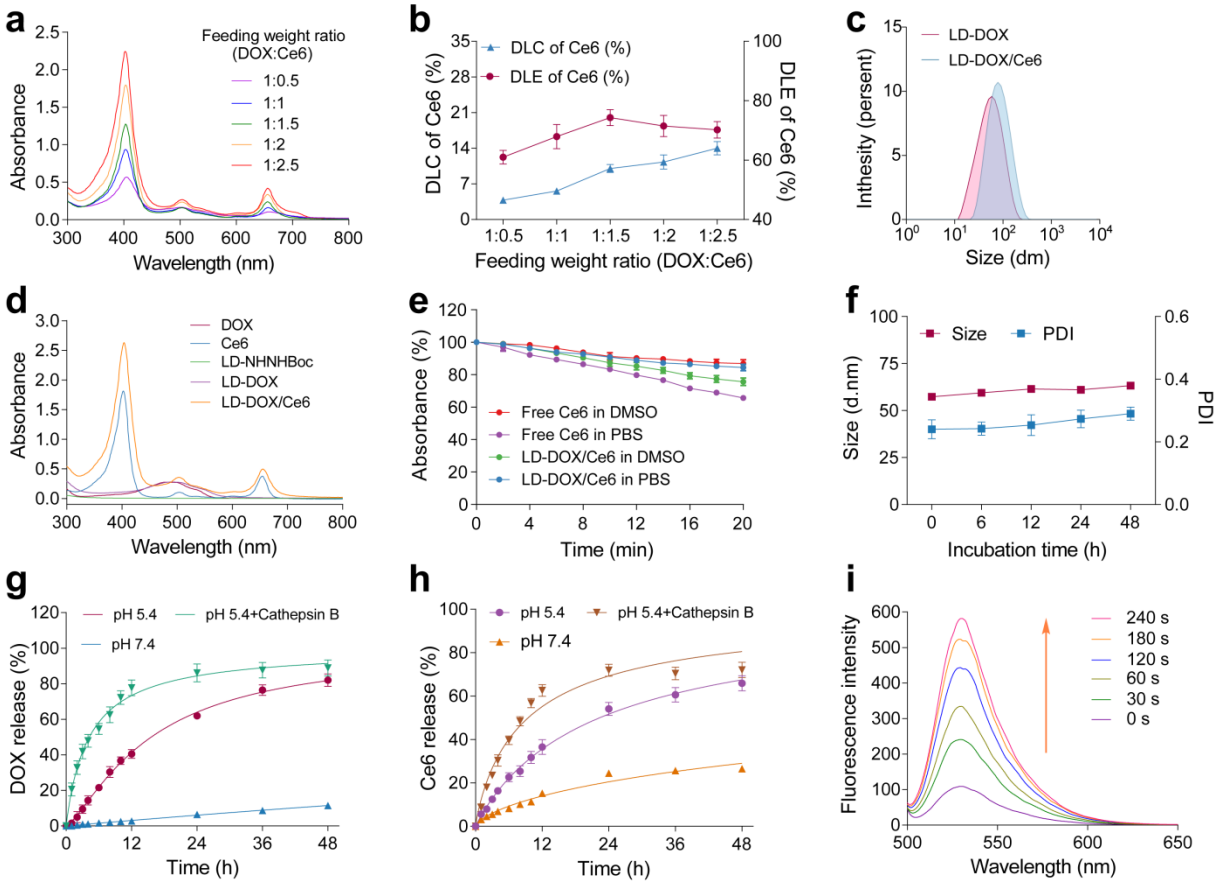



**Figure 2.** Physicochemical characterization of LD-DOX/Ce6. (a) UV-Vis absorption spectra of Ce6-loaded LD-DOX NPs with different feeding weight ratios of DOX to Ce6 in PBS. (b) Drug loading content (DLC) and drug loading efficiency (DLE) of Ce6-loaded LD-DOX NPs with different feeding weight ratios of DOX to Ce6. (c) Size distribution of LD-DOX and LD-DOX/Ce6 as measured by DLS. (d) Absorption spectra of LD-DOX/Ce6 and the controls in PBS (pH 7.4). (e) Photostability of LD-DOX/Ce6 and free Ce6 in DMSO or PBS after laser irradiation (660 nm, 2 mW $cm^{-2}$). (f) Colloidal stability of LD-DOX/Ce6 in PBS at pH 7.4. (g) DOX-release profiles and (h) Ce6-release profiles in the presence or absence of cathapsin B at different pH values. (i) Singlet oxygen generation by LD-DOX/Ce6 NPs under 660 nm laser irradiation (Ce6: 1 μg $mL^{-1}$, 660 nm, 5 mW $cm^{-2}$). Data are expressed as mean ± SD (n = 3).

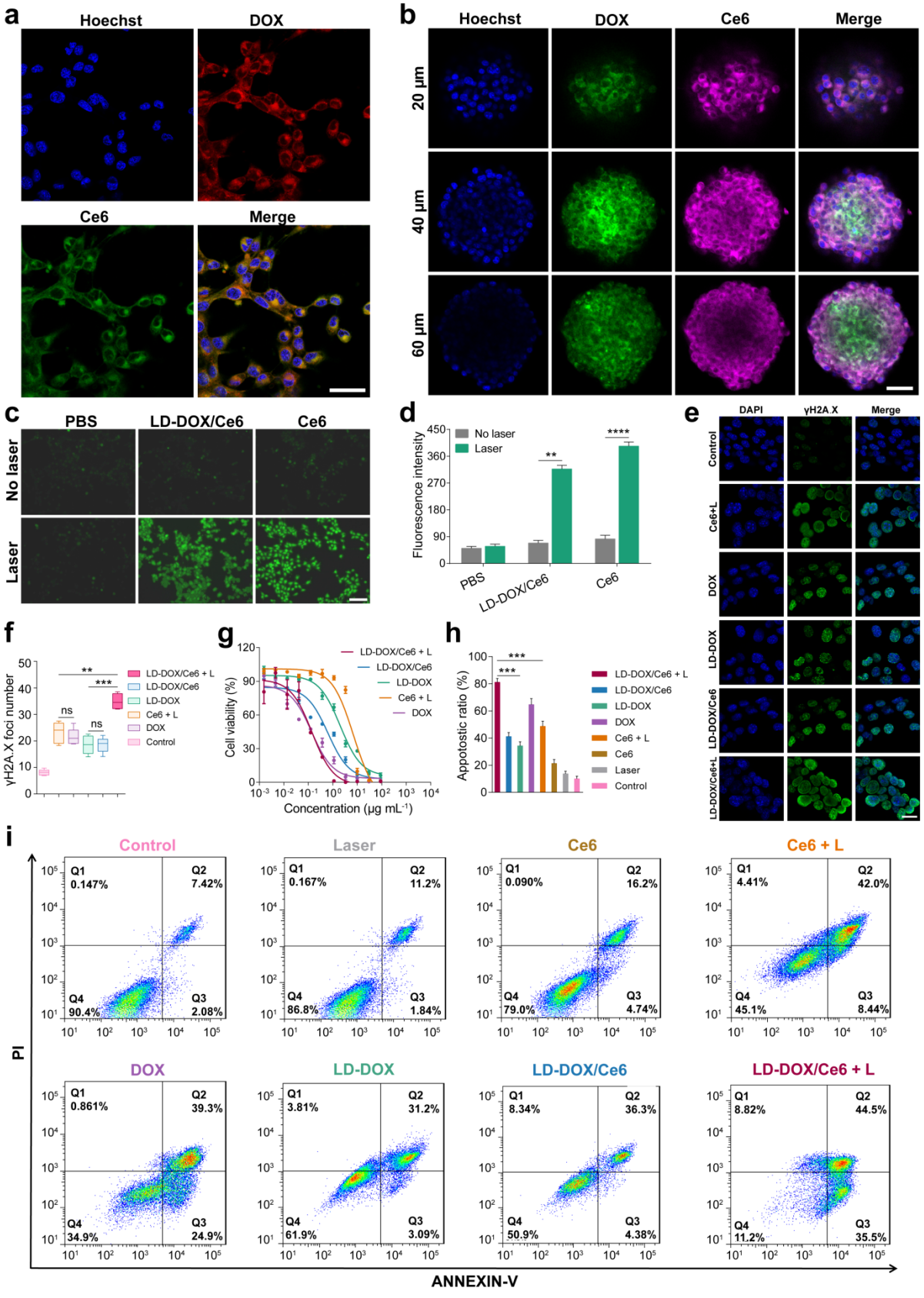



**Figure 3.** (a) Cellular uptake of LD-DOX/Ce6 in 4T1 cells (scale bar = 50 μm). (b) CLSM images of 4T1 three-dimensional multicellular tumor spheroids (MTSs) after treatment with LD-DOX/Ce6 for 6 h (scale bar = 50 μm). (c) Images of 4T1 cells treated with LD-DOX/Ce6 or free Ce6 and then stained using DCFH-

DA to detect ROS generation (scale bar = 100 μm). (d) Quantitative analysis of the mean fluorescence intensity of the ROS probe DCF in 4T1 cells. (e) γH2A.X expression detected by immunofluorescence analysis. Cell nuclei were stained by DAPI (blue) (scale bar = 20 μm). (f) Quantitative analysis of average γH2A.X foci in each cell nuclei. (g) Cytotoxicity of Ce6 + L, DOX, LD-DOX, and LD-DOX/Ce6 against 4T1 cells with or without laser irradiation. (h, i) Flow cytometry analysis of apoptosis in 4T1 cells after treatment with various treatments with or without laser irradiation. Data are expressed as mean ± SD (n=3). $^{****}P < 0.0001$, $^{***}P < 0.001$ and $^{**}P < 0.01$, ns denotes to no significant difference.

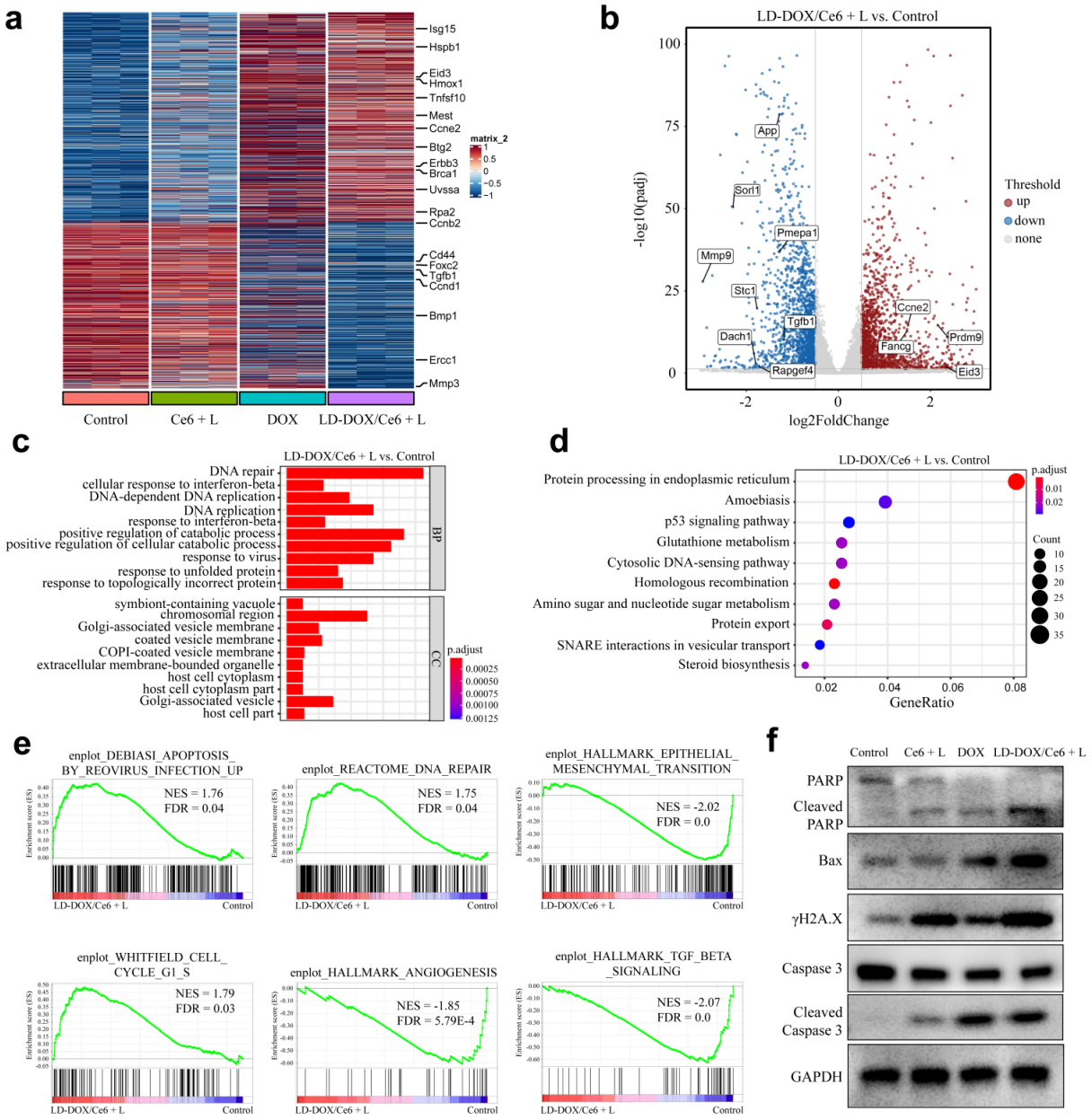



**Figure 4.** (a) Heat map of differentially expressed genes (DEGs) in 4T1 cells after different treatments. (b) Volcano plots of DEGs in 4T1 cells after treatment with control and LD-DOX/Ce6 + L. (c) GO enrichment analysis and (d) KEGG enrichment analysis of the DEGs between LD-DOX/Ce6 + L treatment and control group. (e) Gene Set Enrichment Analysis (GSEA) showing the positive enrichment of the apoptosis, DNA repair, and cell cycle arrest gene signatures, and negative enrichment of the Epithelial-Mesenchymal Transition, angiogenesis, and TGFβ signalling gene signatures in LD-DOX/Ce6 + L comparing to those treated with control. (f) Western blotting plots showing the DNA damage and apoptosis associated markers in 4T1 cells after different treatments.

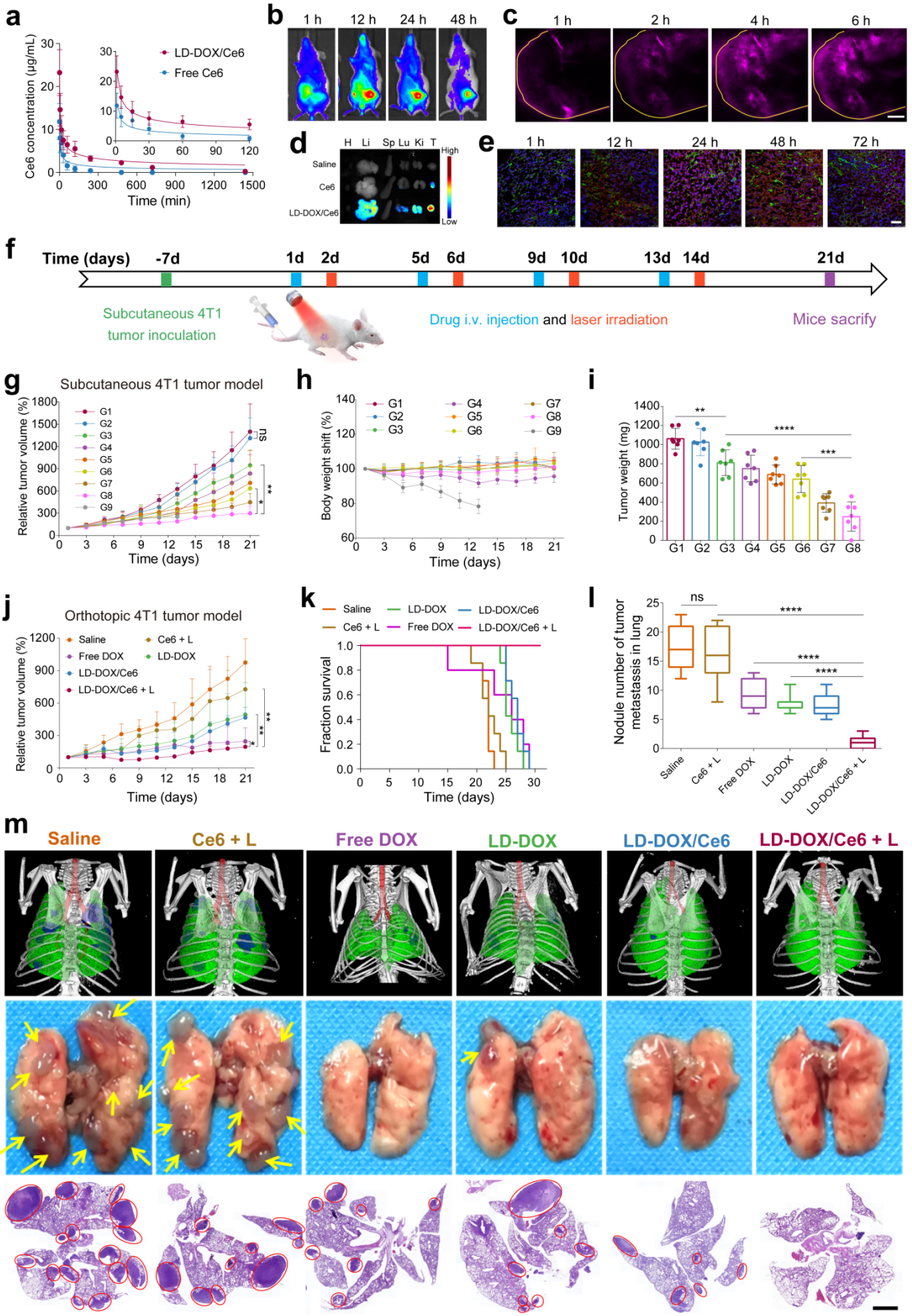



**Figure 5.** (a) Mean plasma concentration of Ce6 in BALB/c mice after i.v. injection with free Ce6 and LD-DOX/Ce6, respective, as determined by measuring the fluorescence intensity of Ce6 in blood at different time points post injection. (b) Representative *in vivo* fluorescence images of the orthotopic 4T1 tumor-

bearing mice after i.v. injection with LD-DOX/Ce6. (c) CLSM images of time-dependent extravasation and penetration of LD-DOX/Ce6 in the orthotopic 4T1 tumor at different time intervals after the injection (tumor tissues indicated by the yellow arrows, scale bar = 200 μm). (d) Representative fluorescence images of the major organs retrieved from the mice 24 h after i.v. injection with LD-DOX/Ce6 (H: heart; Li: liver; Sp: spleen; Lu: lung; Ki: kidney; Tu: tumor). (e) Frozen sections of the tumor visualized by CLSM at various time points after administration of LD-DOX/Ce6 (× 400, scale bar = 50 μm). Green fluorescence was from the anti-CD31 labeled blood vessels, red fluorescence from Ce6 and blue fluorescence from the DAPI-stained nuclei. (f) Treatment schedule for subcutaneous 4T1 tumor-bearing BALB/c mice. The mice were i.v. injected with different formulations, and the tumors were irradiated with laser (660 nm, 250 mW $cm^{-2}$, 20 min) 24 h later. (g) Subcutaneous 4T1 tumor volume growth curves of various formulations with or without laser irradiation. (h) Body weight changes of subcutaneous 4T1 tumor-bearing mice treated by various formulations with or without laser irradiation. (i) Mean tumor weight of mice in each treatment group. (j) Orthotopic 4T1 tumor volume growth curves of various formulations with or without laser irradiation. (k) The survival curves of the orthotopic 4T1 tumor-bearing mice after various treatments. (l) The nodule number of tumor metastasis in lungs at endpoints of the treatments. (m) The lung metastasis of the orthotopic 4T1 tumor-bearing mice after various treatments. From top to bottom: 3D image reconstructed by Micro CT (red, white, green, and blue represent trachea, bone, lung and tumor metastases, respectively), pictures of lungs and H&E staining of lung sections (scale bar = 2 mm). Group 1 (G1): saline; Group 2 (G2): laser alone; Group 3 (G3): free Ce6 + L (8.9 mg Ce6 $kg^{-1}$); Group 4 (G4): free DOX (4 mg DOX $kg^{-1}$); Group 5 (G5): LD-DOX/Ce6 without radiation (4 mg DOX $kg^{-1}$, 4.4 mg Ce6 $kg^{-1}$); Group 6 (G6): LD-DOX/Ce6 without laser irradiation (8 mg DOX $kg^{-1}$, 8.9 mg Ce6 $kg^{-1}$); Group 7 (G7): LD-DOX/Ce6 + L (4 mg DOX $kg^{-1}$, 4.4 mg Ce6 $kg^{-1}$); Group 8 (G8): LD-DOX/Ce6 + L (8 mg DOX $kg^{-1}$, 8.9 mg Ce6 $kg^{-1}$); Group 9 (G9): free DOX (8 mg DOX $kg^{-1}$). ****$P < 0.0001$, ***$P < 0.001$, **$P < 0.01$ and *$P < 0.05$, ns denotes to no significant difference.

**The table of contents**

A novel linear-dendritic block copolymer DOX prodrug with cathepsin B and pH dual-responsiveness was synthesized through a new synthesis strategy. The prodrug and photosensitizer Ce6 self-assemble to form nanoparticles for efficient drug delivery and controlled release drug in tumor cells. DOX and Ce6 exert a synergistic antitumor effect by intensifying cell DNA damage and activating the corresponding apoptotic pathways, resulting in an excellent antitumor effect.

**Keywords:** tumor microenvironment-responsive, linear-dendritic block copolymer, amphiphilic polymer, nanomedicine, combination therapy

Hao Cai, Ping Tan, Xiaoting Chen, Michal Kopytynski, Dayi Pan, Xiuli Zheng, Lei Gu, Qiyong Gong, Xiaohe Tian, Zhongwei Gu, Hu Zhang, Rongjun Chen, Kui Luo*

Stimuli-sensitive linear-dendritic block copolymer-drug prodrug as nano-platform for tumor combination therapy

**ToC figure**

